Towards improving short-term sea ice predictability using deformation observations

Anton Korosov[1], Pierre Rampal[2,1], Yue Ying[1], Einar Ólason[1], and Timothy Williams[1]

[1]Nansen Environmental and Remote Sensing Center, Jahnebakken 3, Bergen, 5007, Norway
[2]CNRS, Institut de Géophysique de l'Environnement, Grenoble, France

Correspondence: Anton Korosov (anton.korosov@nersc.no)

Abstract.

Short-term sea ice predictability is challenging ~~due to the lack of constraints on ice deformation~~despite recent advancements in sea ice modelling and new observations of sea ice deformation, that capture small-scale features (open leads and ridges) at kilometre scale. ~~Deformation observations capture these small-scale features and have the potential to improve the predictability.~~ A new method for assimilation of satellite-derived sea ice deformation into the ~~neXt generation~~ neXt-generation Sea Ice Model (neXtSIM) is presented. Ice deformation provided by the Copernicus Marine ~~Environmental Monitoring~~ Service is computed from sea ice drift derived from Synthetic Aperture Radar at a high spatio-temporal resolution~~of 10 km and 24 hours~~. We show that high values of ice deformation can be interpreted as reduced ice concentration and increased ice damage - scalar variables of neXtSIM. ~~The~~ This proof-of-concept assimilation scheme uses a data ~~nudging approach and deterministic~~ insertion approach and forecasting with one member. We obtain statistics of assimilation impact over a long test period with many realisations starting from different initial times. Assimilation and forecasting experiments are run on ~~example observations from~~ synthetic and real observations in January 2021 and show ~~improvement of neXtSIM skills to predict sea ice deformation in 3–5 dayshorizon~~increased accuracy of deformation prediction for the first 2 – 3 days. It is demonstrated that neXtSIM is also capable of extrapolating the assimilated information in space — gaps in spatially discontinuous satellite observations of deformation are filled with a realistic pattern of ice cracks, confirmed by later satellite observations. ~~The experiments also indicate that reduction in sea ice concentration plays a bigger role in improving ice deformation forecast on synoptic scales.~~ Limitations and usefulness of the proposed assimilation approach are discussed in a context of ensemble forecasts. Pathways to estimate intrinsic predictability of sea ice deformation are proposed.

1 Introduction

Sea ice in the Arctic is continuously drifting and deforming under the influence of atmospheric winds and ocean currents (Sverdrup, 1950; Colony and Thorndike, 1984; Rampal et al., 2009). In summer, when ice concentration is low and ice extent is small, the sea ice is mostly in free drift — the speed and direction of the drift are ~~dictated only~~ dominated by the atmospheric and ocean drag forces and by the Coriolis force. In contrast, in winter the sea ice covers almost the entire Arctic ocean and its adjacent seas, forming a rigid and nearly continuous solid plate. As a consequence, sea ice does not drift freely anymore, but instead exhibits an intermittent ~~and localised drift resulting from complex dynamics driven by a brittle mechanical behaviour. Under~~ drift with localised deformation. First, under increasing external forcing the undamaged ice deforms primarily as an elastic material. Internal stresses ~~may~~ gradually accumulate in the material until a failure criterion is reached, which corresponds to a limit when sea ice fractures~~and~~, and then the ice starts deforming along the multiple narrow and elongated cracks~~formed~~, and does so until these later refreeze or when the load (winds and currents) on the ice changes. Location, density and orientation of these cracks greatly control the overall and individual motion of the resulting ice pieces, from small floes (∼10m) to large plates (∼100km).

Under divergent ice motion these cracks become open leads, significantly increasing ocean-air heat and mass exchange and modifying local atmospheric boundary layer and ocean mixed layer (Olason et al., 2021). Open leads are also key both for marine fauna survival, and for facilitating ship navigation. Under convergent or shear motions sea ice ridges are formed along the cracks. Ridge sails and keels affect the drag by winds and currents. At the same time ridged ice significantly impedes navigation in the Arctic (Lindsay and Stern, 2003).

Given the importance of sea-ice fracturing for air–sea–ice interface processes, marine life and navigation, its accurate monitoring and forecasting is in great demand. Observations of cracks can be performed using satellite remote sensing by retrieval of high-resolution sea ice drift from Synthetic Aperture Radar (SAR) data and computation of sea ice deformation components (Kwok et al., 1990). The Radarsat Geophysical Processor System (RGPS) dataset was the first attempt to systematically observe sea ice drift and derive sea ice deformation on high spatial resolution (10 km) and with high frequency (3 days) over a long period of time (~~winters 1996–2016~~the winters from 1996—2016) (Kwok, 1998). An operational SAR-based sea ice drift and deformation product is currently provided by the Copernicus Marine ~~Environmental Services (CMEMS) (Saldo, 2020). This product~~ Services (Saldo, 2020). It is derived from Sentinel-1 C-band SAR data ~~and has 12 hours frequency and 10 km spatial~~ at 12-hour / 10-km resolution. The cracks appear on satellite-derived ice deformation products as narrow (10 - 30 km, depending on resolution of satellite data) and long (up to 1000 km) lineaments and are also called linear kinematic features (LKFs) (Kwok, 2001).

~~Correct~~ To address the challenge of realistic simulation and forecasting of sea ice dynamics ~~remains a challenge.~~ the next-generation sea ice model (neXtSIM, Bouillon and Rampal, 2015a; Rampal et al., 2016) was developed based on elasto-brittle sea ice rheology (Girard et al., 2011). The spatio-temporal scaling properties of ice deformation are simulated correctly by neXtSIM (Rampal et al., 2019) and the distribution of cracks looks very realistic (Olason et al., 2022). In a recent model intercomparison paper (Bouchat et al., 2021) ~~, only one model, neXtSIM (neXt Generation Sea Ice Model, Bouillon and Rampal, 2015a; Rampa~~ ~~, proved to be capable when run at the same spatial resolution as the available observations (i.e. ∼ 10km) to simulate the~~ neXtSIM results ranked among the best for simulating the observed probability distribution, spatial distribution and fractal properties of sea ice deformation~~. Although the scaling properties of deformation are simulated correctly (Rampal et al., 2019) and the distribution of cracks looks very realistic (Olason et al., 2022), the~~ , even though it operates on a low resolution grid of

10 km. Analysis of spatial and temporal scaling (Fig. 13 in Bouchat et al. (2021)) shows that the spatial structure function of neXtSIM matches the RGPS observations very well, whereas the temporal one is overestimated by 3 – 5 %, probably indicating some overestimation of the intermittency by neXtSIM.

Despite the recent advances in the sea ice modeling, the exact timing and ~~position of~~ spatial distribution (including orientation, width, length and angle of fracture) of strong deformation zones, or LKFs, is not yet predicted precisely. ~~The primary goal of our research is to improve skill in predicting LKFs by assimilating novel satellite observations of sea ice deformation~~Moreover, there are many sources of uncertainty in LKF forecasting that require additional research including: uncertainties in atmospheric and ocean forcing; rheology and model parametrisation; model numerics; initial conditions for sea ice states; observing network and data assimilation. Mohammadi-Aragh et al. (2018) evaluated the potential ~~for predicting~~ predictability of LKFs using an ensemble of sea ice models all using a viscous-plastic rheology, but ~~did not support their findings by observations~~the practical predictability remains unknown.

The primary goal of our research is, therefore, to improve the skill in predicting LKFs by assimilating novel satellite observations of sea ice deformation. Our secondary goal is to quantify the ~~actual~~ practical predictability of LKFs by the neXtSIM model when combined with satellite observations via data assimilation (DA), and study factors affecting it.

Several methodological and technical challenges with assimilating sea ice deformation into a model are worth mentioning here. First, the ~~ice deformation itself~~ “direct insertion" method operates in the model state space. However, the observed deformation is not a model prognostic variable, so ~~the assimilation scheme needs to perform a cross-variable update from deformation to sea ice~~ an operator is used to convert deformation to the model variables. This operator is an inverse of the observation operators used in data assimilation, since it maps from the observation space back to the state space. There is also no guarantee that updated model variables will remain accurate during a forecast. For example, the ice drift is a model variable, but it is strongly dependent on external forcing and increments from assimilation will only survive a short period of time. Second, the observed cracks are very localized in space and time, which pose challenges in ~~modeling~~ modelling its covariance structure for data assimilation methods such as 3DVar (Lorenc, 1986). Ensemble Kalman filter (EnKF) (Evensen, 2003) is potentially a good solution through estimating a flow-dependent covariance structure from an ensemble of model runs. However, the current ensemble ~~DA~~ data assimilation framework for neXtSIM (Cheng et al., 2020) is not ready to assimilate deformation yet. Therefore, and also as a proof of concept, we present here a first attempt to assimilate sea ice deformation into neXtSIM using a simple ~~nudging scheme~~ direct data insertion scheme (Stanev and Schulz-Stellenfleth, 2014), and perform a sensitivity analysis useful for demonstration of the approach.

The concept of sea ice deformation assimilation is presented in Section 2, followed by a detailed description of satellite observations of deformation and the methodology for assimilation and running forecasting experiments in Section 3. The results are presented and discussed in Sections 4 and 5.

2 Link between observed ice deformation and model state

The central idea in our assimilation approach is that the ice in the model should become weaker — in a mechanical sense — where high deformation is observed. In the current context, we simulate sea ice "weakness" evolution according to the Brittle Bingham-Maxwell (BBM) rheology (see (Olason et al., 2022) for details on how this rheology is implemented into neXtSIM). BBM belongs to a family of brittle rheologies, with earlier variations being the Elasto-Brittle (EB) (Girard et al., 2011) and the Maxwell Elasto-Brittle (MEB) (Dansereau et al., 2016). Two regimes are distinguished in the BBM: the undamaged pack ice can have small elastic (reversible) deformations; in the cracks the deformation is visco-elastic (partly permanent and partly reversible) and can become quite high (e.g. several percent per day over a spatial scale of about 10 km). The BBM stress evolution equation writes as follows:

$$\dot{\sigma} = E\mathbf{K} : \dot{\varepsilon} - \frac{\sigma}{\lambda}\left(1 + \widetilde{P} + \frac{\lambda \dot{d}}{1-d}\right), \tag{1}$$

where σ is the internal stress tensor, E is the ice elasticity, $K : \dot{\varepsilon}$ is the stiffness tensor, $\lambda = \eta/E$ is the viscous relaxation time, $\widetilde{P}$ is a generalised friction term, d is the ice damage (with $d = 0$ being completely undamaged ice).

Elasticity and viscosity are functions of the model state variables damage (d) and concentration (A):

$$E = E_0(1-d)e^{-C(1-A)} \tag{2}$$

$$\eta = \eta_0(1-d)^{\alpha}e^{-\alpha C(1-A)}, \tag{3}$$

where E_0 and η_0 are the undamaged elasticity and viscosity, and $\alpha > 1$ is a constant.

$\widetilde{P}$ contains the effects of the friction element and is defined as:

$$\widetilde{P} = \begin{cases} \frac{P_{\max}}{\sigma_n} & \text{for } \sigma_n < -P_{\max}, \\ -1 & \text{for } -P_{\max} < \sigma_n < 0, \\ 0 & \text{for } \sigma_n > 0. \end{cases} \tag{4}$$

The friction element is active when damaged ice is converging (i.e., when the normal stress σ_n<0); when ~~$\sigma_n = -P_{max}$~~ $\sigma_n = -P_{\max}$, the frictional forces can no longer balance the convergence and the ice starts to ridge. This threshold is defined as:

$$P_{\max} = Ph^{3/2}e^{-C(1-A)}, \tag{5}$$

where P is a constant scaling parameter for the ridging threshold to parameterise $P_{\max}$, following the results of Hopkins (1998) , and h is thickness.

Eqs. 2, 3, 5 show that increasing damage (d) will decrease viscosity, while decreasing concentration A will both decrease viscosity and shift the threshold $P_{\max}$, so that the ice transitions from the elastic to the viscous regime and ~~will allow~~ allows larger deformations without significant increase in internal stress.

~~As explained in detail in Section 3.4 we~~ We use an empirical function to convert the observed deformation to model variables, so that the update can take place in the model state space. The ~~"observed" variable v_o (damage or concentration) is computed from observed deformation ϵ_o~~ "observed" model variables damage d_o and concentration A_o are derived from the observed deformation ε_o using the following experimental formulations:

$$d_o = \cancel{f}\,H'_d(\varepsilon_o) \tag{6}$$

$$A_o = \cancel{f}\,H'_A(\varepsilon_o) \tag{7}$$

where H'_d and H'_A are inverse observational operators (see Section 3.3 and Appendix 1).

3 Data and Methods

3.1 Satellite observations of sea ice deformation

We used the sea ice drift and deformation dataset from ~~CMEMS~~ Copernicus Marine Services (Saldo, 2020) acquired in January 2021. The dataset comprises gridded products derived from Sentinel-1 synthetic aperture radar (SAR) images, with 10 km spatial resolution~~and~~. Ice drift is computed from pairs of images separated by approximately 24 hours and the product is delivered every 12 hours~~frequency~~. The spatial coverage of the product is irregular - the East Siberian, Laptev and Kara ~~sea~~ seas and the polar gap (north of 87°N) are never covered, while other Arctic regions are observed ~~nearly every day~~at least once nearly every 24 hours.

3.2 Simulation experiments setup

The model is run using a ~~900 seconds~~ 900-s time step on a triangular mesh with 10 km spatial resolution covering the Arctic ocean and adjacent seas north of 65°N. The model is forced with the ~~European Centre~~ latest version (Cycle 45r1) of the Integrated Forecast System European Center for Medium-Range Weather Forecasts (ECMWF) ~~operational analysis (Zuo et al., 2019) atmospheric forcing fields (wind speeds, air temperature, precipitation, humidity)~~ (Owens and Hewson, 2018) and the TOPAZ4 (Sakov et al., 2012) ocean forcing fields (currents, sea surface temperature, sea surface salinity).

~~The model is initialised on~~ Experiments start from 1 December 2020 ~~from TOPAZ4 sea ice concentration, thickness, snow thickness and is run~~ (t_0) and last for two months. ~~Other~~ Let $\mathbf{x}$ denote the model state variables (~~damage, temperature, etc) are set to a constant value.After a 30-day spin-up the concentration, thickness and deformation fields reach an equilibrium and the period from 1st to 31st Jan~~ e.g., concentration, damage, drift, etc.), $\mathbf{x}_{t_0}$ is the initial condition, and $M_{t_n \to t_{n+1}}$ is the non-linear model (neXtSIM) to propagate state from time t_n to t_{n+1}.

Let $\mathbf{y}$ denote the observations (ice deformation rate), which is related to the model state variables through $\mathbf{y}_t = H(\mathbf{x}_t)$, where H is the observation operator. Real satellite observations $\mathbf{y}_t^o$ are available throughout the test period. Although the deformation rate is derived from sea ice drift, derived from Radarsat-2 SAR images, we call them "observations of deformation" as opposed to "simulation of deformation" by neXtSIM.

In the first experiment a verifying "truth run" is generated:

$$\mathbf{x}_t^{\mathrm{tr}} = M_{t_0 \to t}(\mathbf{x}_{t_0}) \tag{8}$$

The period before 1 January 2021 is used for analysis as a spin-up time, the data from $\mathbf{x}_t^{\mathrm{tr}}$ is not used, and time t_1 denotes the 1 January 2021. Then four sets of 10-days forecasts are initialised and ran every day in January 2021, so that each set has 31 forecast (see scheme on Fig. **??**). The forecast runs are initialised every day in January 2021 from the assimilated damage and concentration variables and other variables from the free run. Forecasts are produced every day for a period of 5 days.1).

Scheme of the spin up run (gray curve), free run (blue curve) and forecasts (green curves). Time scale is not preserved. **1. Forecasts initiated from truth**:

$$\mathbf{x}_{t_1 \to t}^{\mathrm{T}} = M_{t_1 \to t}(\mathbf{x}_{t_1}^{\mathrm{tr}}) + \boldsymbol{\psi}_t, \tag{9}$$

where $\boldsymbol{\psi}_t$ is a random noise due to uncertainties in model numerics that cause the forecasts run to differ from the truth run. These forecasts are evaluated by computing the error in observation space:

$$\epsilon_{\delta t}^T = \left\langle H(\mathbf{x}_{t \to t+\delta t}^T) - H(\mathbf{x}_{t \to t+\delta t}^{tr}) \right\rangle \tag{10}$$

where $\langle \cdot \rangle$ denotes averaging over the different forecasts starting from $t_1, t_2, \ldots, t_n$, i.e. $\langle \epsilon_{t \to t+\delta t}^T \rangle = \sum_{t=t_1}^{t_n} \epsilon_{t \to t+\delta t}^T$, then plotted w.r.t. lead time δt.

For initialising a forecast run at time **2. Forecasts without data assimilation:**

$$\mathbf{x}_{t_1 \to t} = M_{t_1 \to t}(\mathbf{x}_{t_1}) + \boldsymbol{\psi}_t \tag{11}$$

The first forecast is initiated from t_0 from assimilated damage and concentration, the deformation is taken from satellite observations of drift between times t_0 and , subsequent forecasts are initiated from the outputs of the previous forecasts. The forecasts initiated during the spin-up period are not used. The forecasts after 1 January are evaluated against truth:

$$\epsilon_t^B = H(\mathbf{x}_t) - H(\mathbf{x}_t^{tr}) \tag{12}$$

and against real observations:

$$\epsilon_t^O = H(\mathbf{x}_t) - \mathbf{y}_t^o \tag{13}$$

During the spin-up period ϵ_t^B grows and reaches its saturation level ϵ_B, which we consider to be the climatological level for this error. Since the forecasts without data assimilation don't see real data, the error ϵ_t^O averaged over one month (ϵ_O) can also be considered as the climatological level.

3. Forecasts with assimilation of synthetic data:

$$\mathbf{x}^{as}_{t_1\rightarrow t} = M_{t_1\rightarrow t}(\mathbf{x}^{as}_{t_1}) + \boldsymbol{\psi}_t \quad (14)$$

where $\mathbf{x}^{as}_{t_1}$ is the analysis of synthetic observations from the truth run and the forecasts without assimilation performed at t_1~~separated by 24 hours (see scheme in Fig. ??). For evaluation,~~ : $\mathbf{x}^{as}_{t_1} = A(\mathbf{x}_{t_1}, \mathbf{y}^{tr}_{t_1}; H', \mathbf{w})$. In the assimilation scheme in this paper, we use the inverse operator H' to compute model state (concentration and damage) from the observed deformation, $\mathbf{x}_t = H'(\mathbf{y}_t)$ (see Eqs. 6 and 7 for how H' is constructed) and $\mathbf{w}$ are the tuning parameters (see Eqs. 22 for how A is constructed). These forecasts are evaluated with:

$$\epsilon^{S}_{\delta t} = \left\langle H(\mathbf{x}^{as}_{t\rightarrow t+\delta t}) - \mathbf{y}^{tr}_{t+\delta t}\right\rangle \quad (15)$$

4. Forecasts with assimilation of real satellite data:

$$\mathbf{x}^{ar}_{t_1\rightarrow t} = A(\mathbf{x}_{t_1}, \mathbf{y}^{o}_{t_1}; H', \mathbf{w}) \quad (16)$$

evaluated with:

$$\epsilon^{A}_{\delta t} = \left\langle H(\mathbf{x}^{ar}_{t\rightarrow t+\delta t}) - \mathbf{y}^{o}_{t+\delta t}\right\rangle \quad (17)$$

It should be noted that for assimilation the deformation is computed from observations of drift at $t_{n-1} \rightarrow t_n$ and the model is initialised from the analysis at time t_n. Then the forecast is compared with deformation computed at $t_n \rightarrow t_{n+1}$, $t_{n+1} \rightarrow tn+2$, etc. Thus, the ~~deformation is computed from the forecasted drift between two dates separated by 24 hours (e. g., t_0 and t_1, or t_1 and t_2) and compared with observed deformation corresponding to the same time period. Observations (and corresponding evaluations)between t_0 and t_1 are hereafter denoted as having zero lead time . The deformation components (divergence, shear, vorticity, total, denoted as ε_{div}, ε_{shr}, ε_{vor}, ε_{tot}) are computed from the simulated drift using contour integrals of velocities over the triangular elements of the model's mesh as explained in the previous work of (e.g. (Bouillon and Rampal, 2015b)~~error of the forecast $\epsilon^{A}_{t_n\rightarrow t_{n+1}}$ is independent from observations used in assimilation $\mathbf{y}^{o}_{t_{n-1}\rightarrow t_n}$ (the same holds for $\epsilon^{S}_{\delta t}$).

3.3 ~~Data assimilation method~~

Predictability is defined as the time at which a forecast error reaches a background level (Zhang et al., 2019). Since the errors of the forecasts without assimilation ϵ_B and ϵ_O are at their respective saturation levels, we assume them to be the background levels for the forecasts with assimilation. Therefore, in a perfect-model scenario (forecast with initialisation from truth) the intrinsic predictability is the time δt when $\epsilon^{T}_{\delta t} \approx \epsilon_B$. The practical predictability is the time δt when $\epsilon^{S}_{\delta t} \approx \epsilon_B$. Similarly, in the case of assimilation of real observations the practical predictability is time δt when $\epsilon^{A}_{\delta t} \approx \epsilon_O$.

~~The function $f_d()$ (Eq. 6 in Section 2) is established from the following considerations. A true relationship between deformation and model variables is multivariate and involves nonlinear dependencies on the external forcing: even fully-damaged ice will not deform without winds or currents. Satellite observations and our previous studies with the neXtSIM model show~~

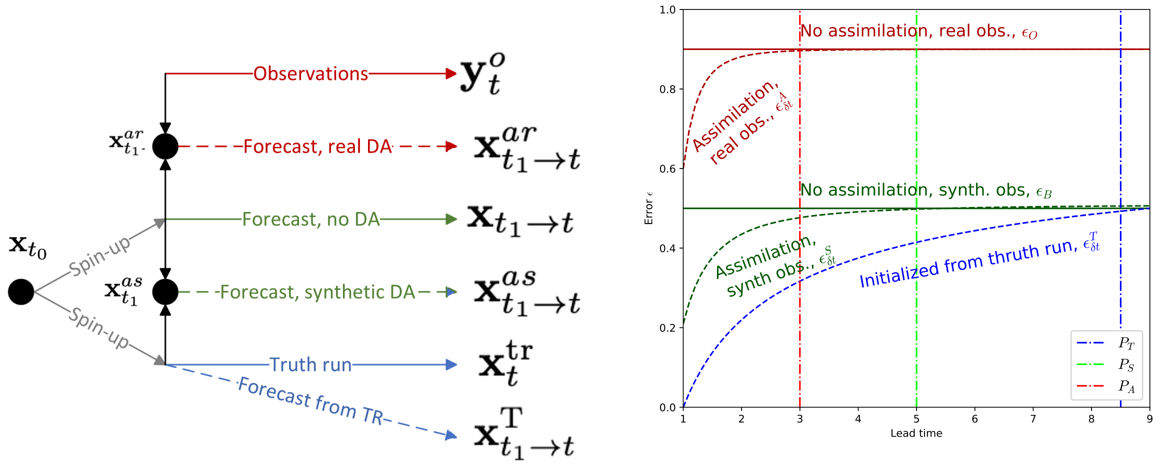

Figure 1. Scheme of assimilation experiments (orange circleleft) and evaluation scheme of errors (purple circleright). The truth run is shown by solid blue line, observations - by solid red line. The forecasts initiated from the truth - dashed blue line; without assimilation - solid green line; with assimilation of synthetic observations - dashed green line; with assimilation of real satellite observations - dashed red line. Grey lines show spin-up period for the truth and the no-DA forecasts(. On the scheme of errors the lines are coloured as follows: red - evaluation against satellite observations, green arrow) using - evaluation against synthetic observations(black arrow), blue - evaluation against the "truth run". EpsSolid lines show climatological level, d dashed - average over forecasts. Vertical lines P_T, P_S and A denote deformationP_A indicate potential predictability, damage practical predictability for synthetic DA and concentration practical predictability for real DA, correspondingly.Subscripts F and O denote forecast and observation.

that the values of ice deformation follow a log-normal distribution (Marsan et al., 2004; Rampal et al., 2019). As detailed in the supplementary materials (see Appendix I) our simulations show that a log-normal function can accurately describe the distribution of $(1-d)$. Damage's distribution has a mean about 0.95 and exhibits a short tail towards 1 and a relatively longer tail towards smaller values. Our simulations also show a linear relationship between damage and total deformation in log-log space, i.e.: Our previous experiments (Williams et al., 2021) showed that assimilation of concentration is not significantly affecting accuracy of sea ice drift forecast. In that sense the reference forecasts without DA ($\mathbf{x}_{t_1\to t}$) are almost equal to the forecasts with assimilation of concentration, and the error ϵ_A helps to evaluate the general improvement due to the DA system.

$$\log_{10}(k_1+1-d) = k_2 + k_3\log_{10}(\varepsilon_{tot})$$

3.3 Inverse observational operator

where k_2 and k_3 are linear regression coefficients and k_1 is a small offset to prevent damage getting too close to The inverse observational operator H' is a function to compute a model state variable from observations: $\mathbf{x} = H'(\mathbf{y})$. Since reliable simultaneous observations of concentration and deformation at scales of 1 (a value that damage should never reach in progressive damage r . The expression for computing damage is thus:

$$d = f_d(\varepsilon_{tot}) = 1 - 10^{k_2 + k_3 \log_{10}(\varepsilon_{tot})} - k_1$$

The coefficients k_1, k_2 day / 10 km are not available, and k_3 are found experimentally following two steps (see Appendix I for details). First, both the model damage (d_M) and deformation (ε_M) are taken from the free run and the preliminary coefficient values are found using the least squares method. Seconddamage is not an observable variable, we had to use the data from model runs for defining the H' parameters. Another reason is that the assimilated weakening of sea ice (by insertion of decreased A or increased d) must be consistent with the model parameterisation. For example, if observations showed a higher rate of concentration decrease per unit deformation rate than we obtain from simulations, then the assimilation would decrease the concentration too much, and the model would predict higher deformation than was actually observed.

In our experiments, the deformation is taken from the satellite observations (ε_O)and damage is computed using the preliminary coefficients $d_O = f_d(\varepsilon_O; k_1, k_2, k_3)$. Then the frequency distributions of the model damage (d_M)and the reconstructed damage (d_O) are compared and the coefficients k_1, k_2 and k_3 are updated by fitting these distributions. The latter step is required due to the initial differences existing between the simulated and observed frequency distributions of deformation that result from varying integration time of satellite observations, noise in observations, anduncertainties in simulated drift. computed in each model mesh element by integrating ice drift velocities simulated in the truth run over a period of 24 hours ($t_{n-1} \rightarrow t_n$):

$$\mathbf{y}_{t_n} = \varepsilon_{t_n} = H(\mathbf{x}_{t_{n-1} \rightarrow t_n}) \tag{18}$$

The function $f_A()$ in Eq. 7 in our assimilation scheme has a simpler form:

$$A = f_A(\varepsilon_{tot}) = 1 - a_1 \varepsilon_{tot}$$

Then H' is applied to $\mathbf{y}_{t_n}$ for computing damage and concentration, and the results are compared to the simulated damage and concentration in the corresponding elements at the end of this period (t_n). The initial values of H' parameters are found by minimisation:

$$H' = \underset{H'}{\operatorname{argmin}} \left(\sum_{n=1}^{30} \left[H'(\mathbf{y}_{t_{n-1} \rightarrow t_n}) - \mathbf{x}_{t_n} \right]^2 \right) \tag{19}$$

It can be justified by the fact that in case of pure divergence the decrease in concentration is a product of divergence rate (ε_{div}) and time, therefore the coefficient a_1 has a meaning of integration time. However in Eq. 21 we compute deformation from where n denotes day number in the truth run.

The total deformation (ε_{tot}~~assuming that ice breaks and should become weaker also in case of convergence or shear. The coefficient a_1 is found empirically through the sensitivity experiments described below.~~ , m^{-1}) is used as a predictor for damage and concentration under the assumption that all deformation events (convergence, divergence and shear) indicate the presence of weaker ice that may continue to be deformed. Ice weakness is simulated in neXtSIM by decreased concentration or increased damage (see Eqs. 2 and 3). Observation of any deformation components (including convergence) is interpreted in the assimilation procedure as an increase in ice weakness and, therefore, a decrease in concentration or an increase in damage. We therefore suggest that the total deformation is a good proxy for the presence of weak ice and a single dependence of A and d on the total deformation can be used.

It should be added, that there are two ice categories in the model: older ice, whose concentration is used in rheology and younger ice, which is formed during water freezing and is converted to older ice only after exceeding a threshold in thickness. Only the older ice is updated in the assimilation procedure and the total ice concentration remains the same.

The inverse operators for damage and concentration have the following form (for further details see Appendix 1):

$$H'_d(\varepsilon_{tot}) = 1 - 10^{k_2 + k_3 \log_{10}(\varepsilon_{tot})} - k_1 \tag{20}$$

$$H'_A(\varepsilon_{tot}) = 1 - a_1 \varepsilon_{tot} \tag{21}$$

3.4 Data assimilation method

We update the damage and concentration variables in the model according to the observed deformation using a simple ~~least-squares nudging~~ "direct data insertion" approach as a proof of concept for DA (Stanev and Schulz-Stellenfleth, 2014). The updated state variable is computed as a weighted average of the forecasted variable (~~v_m~~$\mathbf{x}$) and the variable computed from the observed deformation (~~v_o):~~

$\mathbf{x}^o = H'(\mathbf{y}^o)$):

$$v_a \mathbf{x}^a = w * v_o \mathbf{x}^o + (1-w) v_m \mathbf{x} \tag{22}$$

where w is the weight applied to observations.

As defined here, the weight can be interpreted as ~~precision (inverse of~~ the precision (the inverse of the uncertainty) of ~~observation~~ the observed relative to the ~~model~~ modelled variable. In variational assimilation schemes the uncertainties are characterised by error co-variance matrices, while here we assume no correlation structure between variables and only characterise the relative precision (signal to noise ratio of observation-to-model variable error variances) as a single weight. ~~Though simplified, we~~ However, we still allow this weight to be individually specified for different variables and also to be spatially varying, ~~therefore giving~~ giving some more flexibility to the update scheme. Also, we note that we assume the model variables are spatially uncorrelated, and that the variable on each model mesh point can be updated independently. ~~Considering that~~ Since sea ice deformation is accommodated along nearly 1D geometrical features (i.e. fractures), ~~the very small spatial correlation approximation~~ correlation can only usually be seen along the fracture, and so assumption of low spatial correlations in all other directions is reasonable.

We parameterize the weights as:

$$w = w_v W \tag{23}$$

where w_v is a variable specific weight (either w_d or w_A) and W is ~~weight~~ a weight that is dependent on observed deformation:

$$W = \begin{cases} 1, & \text{if } \varepsilon > \varepsilon_{min}, \\ 0, & \text{otherwise} \end{cases} \tag{24}$$

where ε_{min} is a threshold for total deformation ~~.~~
found in sensitivity experiments. It is known that low values of deformation have higher uncertainty (Dierking et al., 2020), so it is sensible to update model variables only when the observed deformation exceeds the threshold value. This threshold localizes the impact of assimilating observed deformation to only be effective in the vicinity of ice cracks.

The variable-dependency is tested by setting the weight as 0 or 1 for damage and concentration~~(~~, i.e., letting assimilation update only damage or concentration, or both to see the impact of the update~~)~~.

3.5 Sensitivity experiments

The list of parameters tested in the sensitivity experiments is provided in Table 1. ~~Since it was difficult to distinguish between the individual impacts of w_v and W in Eq. 23, only values of 0 and 1 were tested for w_d and w_A, thus enabling or disabling assimilation of damage and concentration in the experiments.~~ The values for a_1 and ε_{min} were tested within reasonable ranges, i.e. expected decrease of concentration due to ice deformation given the observable ranges of deformation.

Table 1. Tested parameters of sea ice deformation assimilation scheme

Parameter	Description	Eq.	Tested values
a_1	Coefficient for computing sea ice concentration from deformation	21	0.1, 0.3, 0.5, 0.9, 1.2, 1.5, 2
w_d	Weight of damage assimilation	23	0, 0.5, 1
w_A	Weight of concentration assimilation	23	0, 0.5, 1
ε_{min}	Threshold of total deformation for applying assimilation	24	0.01, 0.02, 0.1

Over 30 experiments were run following the algorithm:

- Choose assimilation parameters from a predefined space and save in a configuration file
- Run a series of 31 forecasts in January 2021 with these parameters
- Evaluate each forecast by comparing simulated and observed deformations
- Average the evaluated quality metrics over the month

The effect of assimilation on the prediction skill is evaluated by comparison of the simulated and observed deformation fields. As mentioned above, ice deformation is related to the processes of ridging and lead opening and, therefore by using the deformation as the reference we evaluate the model skills to correctly predict leads and ridges - total deformation fields as it is crucial information for safe navigation, ecological and climate studies.

The forecasts were The forecasts are evaluated using two quality metrics: area of maximum cross-correlation (MCC) and difference in 90th percentile, hereafter referred to as A_{MCC} and D_{P90}. The), and difference in probability distributions of total deformation (KS).

A_{MCC} is computed as the area where the maximum cross-correlation (see Korosov and Rampal, 2017, for explanation) between the observed and simulated deformation was computed in a sliding window of 20 x 20 pixels (200 x 200 km)and the maximum value from the cross-correlation matrix was preserved for each floating window (see Fig. ?? for an example of MCC) . The area where the MCC (MCC, see Appendix 2 for details) is above 0.35normalised to , normalised by the total area of available satellite observationswas considered as one quality metric for one deformation field's forecast. This metric . A_{MCC} indicates the level of correspondence spatial collocation of forecast LKFs to observations at a relatively fine spatial scale (1 - 2 pixels, 10 - 20 km). Unlike the LKF evaluation metrics suggested in (Hutter et al., 2019), that compare only statistical properties of LKFs (number, density, length, orientation, etc), the MCC-based metric estimates co-alignment of individual LKFs on model simulations and satellite observations. It is also thought to be more sensitive to LKFs with low deformation magnitude, as no threshold is applied for their detection.

For calculating the other quality metrics the 90th percentile was computed from observed and simulated deformations in the same sliding window. Then the root mean square difference of P90 values is computed from the entire deformation field in order to quantify the match between the model and satellite observations at the basin scale. KS is the difference between PDFs of ε_{tot} computed using the Kolmogorov-Smirnov test (Smirnov, 1939), and indicates the correspondence of the magnitude of the predicted deformation to observations on pan-Arctic scale.

4 Results

4.1 Impact on fields of concentration and damage

Fig. 2 shows example fields of sea ice deformation computed from ice drift between 15 and 16 January and also the corresponding damage and concentration fields computed during the assimilation procedure using the following values: $\varepsilon_{min} = 0.02$, $w_d = 1$, $w_c = 1$, $a_1 = 0.9$. White gaps on the field of deformation (Fig. 2, A) show areas without satellite data coverage. The white gaps on the reconstructed concentration and damage maps are also due to application of the ε_{min} threshold - values of ε_{tot} below that threshold are not used in assimilation.

The range of the reconstructed concentration corresponds well to the simulated one. Only the largest cracks with deformation above 0.3 d^{-1} have concentration below 0.7, while the other cracks have a realistic values of concentrations in range 0.9 - 1 if compared, for example, to the AMSR2 sea ice concentration product from the Ocean and Sea Ice Satellite Application Facility (EUMETSAT, 2021). The pattern of LKFs, exhibited as reduced concentrations, in general looks similar to the simulated field, but the exact position is, of course, different. It also seems that there are more reconstructed LKFs than the simulated ones. It can be explained by the fact that the simulated concentration only decreases in the case of divergence, whereas the reconstructed LKFs are a function of total deformation. The analysis produces a reasonably looking field of concentration that should not shock the model.

Similar conclusions can be drawn regarding the damage fields. The only observed difference is that the simulated damage is so spatially heterogeneous that contributions from the “observed” damage are difficult to spot on the analysis field.

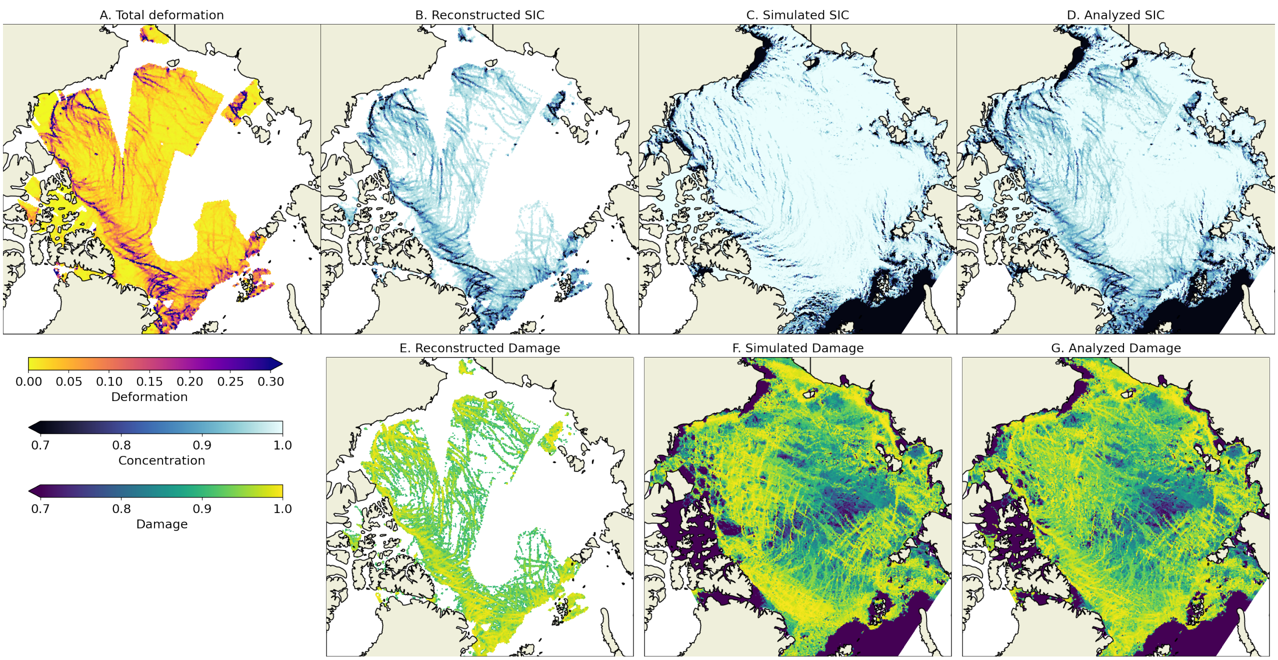

Figure 2. A: sea ice deformation (d^{-1}) computed from observed ice drift between 15 and 16 January 2022 and corresponding damage and concentration fields. B and E: A and d reconstructed from the deformation, C and F: simulated by neXtSIM, D and G: results of analysis.

4.2 Impact of assimilation on deformation fields

The impact of assimilation is demonstrated by a comparison of sea ice deformation maps from observations on 22^{nd} January 2021 deformation fields from a 3-day forecast without DA (Fig. ??.A), a free run without assimilation (Fig??. B)3, first column), from observations (Fig. 3, second column), and a forecast with assimilation of concentration computed from deformation (Fig??. C). In that example only concentration was updated with $a_1 = 1.2$, $w_A = 1$, and $\varepsilon_{min} = 0.02$. Other assimilation parameters are tested below in Section 4.4. FigDA (Fig. ?? 3, third column). The assimilation was performed on 16 January (see Fig. 2 for corresponding fields of damage and concentration). The fourth column shows the MCC computed between the observation and the forecast with DA, where insignificant correlations are masked with white colour. In the fifth column the increase of MCC ($MCC_{Increase} = MCC_{DA} - MCC_{NODA}$) is shown as an indication of areas where DA improved location of the LKFs.

Fig. 3 clearly shows that the field of deformation predicted in the free run (Fig ??.B) without DA is different from the observations both in terms of location, sharpness and orientation of cracks, as well as in terms of the deformation magnitude. The corresponding maximum cross correlation map (Fig ??.C) shows very low values (average correlation is 0.2) and the map of P90 difference (Fig ??.D) confirms strong underestimation of total deformation (mostly < -0.1 d^{-1}).

After first day after assimilation the field of deformation changes substantially where the observations were present (such area on Fig ??. C is highlighted). predicted deformation is substantially different from the no-DA run. Visually the position of cracks correspond well to the observations, which is supported by high values of correlation (the average correlation is 0.7 , Fig. ??.F) and low difference of P90 (average D_{P90} is 0.01 d^{-1}, Fig. ??.G). We also note that the deformation field changes outside the area of assimilation (semi-transparent regions on Fig. ??.B and ??.C). For example, cracks near the North Pole change orientation by 45 degrees, the cracks north-east of the New Siberian Islands (next to — see Fig. 3, fourth column) and MCC is higher in the DA-forecast in most of the observed areas (the Beaufort, Chuckhi, Lincoln seas). On the second day, while both forecasts start to look more similar, the MCC with observations is still high in many areas, but an increase of MCC is visible only in parts of the observations) disappear, many features in the Beaufort seareduce intensity or disappear. Thus, due to its rheology, neXtSIM is able to extrapolate and create realistic connections between the observed and assimilated pieces of LKFs. On the third day the improvement introduced by DA is obvious only in the central Arctic, on intersection of two large cracks crossing the entire ocean.

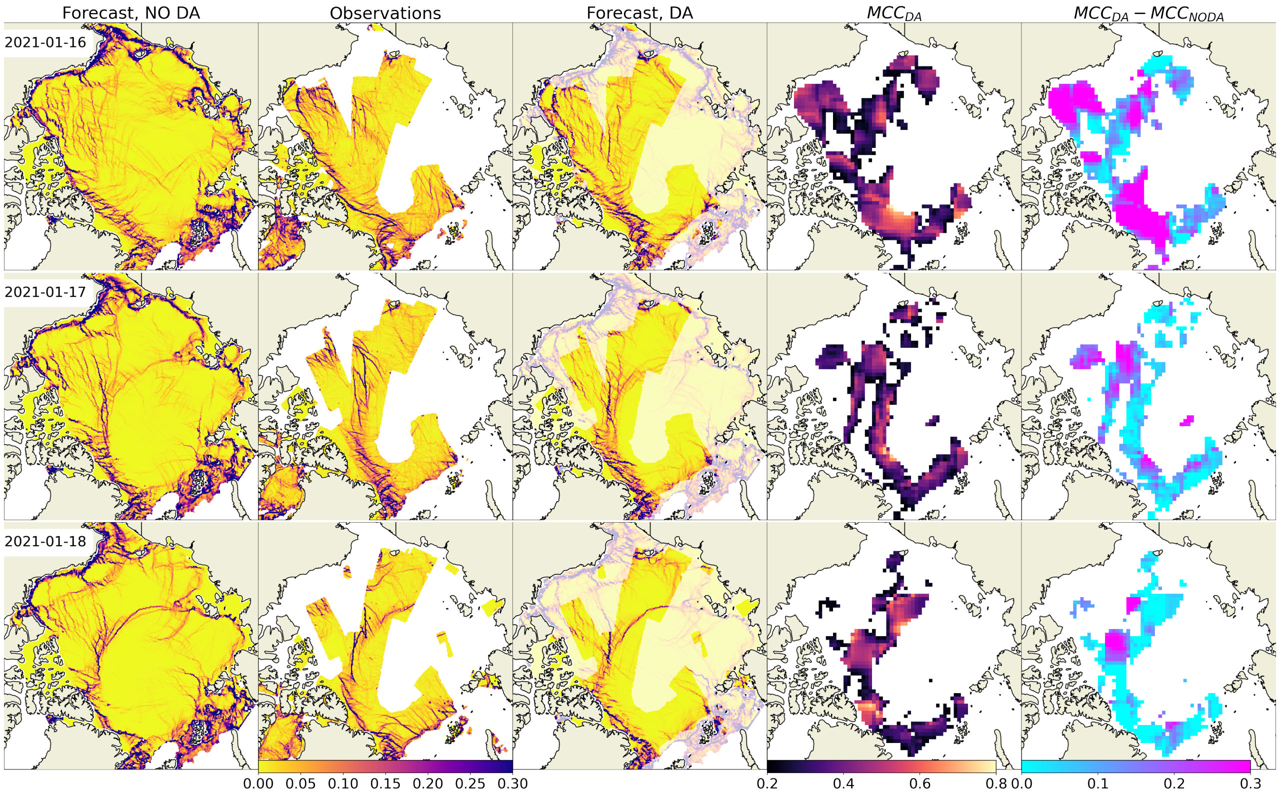

Figure 3. Maps of sea ice total deformation ~~showing impact of assimilation~~(d^{-1}) and their comparison. ~~A -~~ Column 1: forecast without DA; Column 2: observations~~on 22 January 2021. B - free run. C -~~ ; Column 3: forecast with ~~assimilation of deformation with zero days lead time. D - map of maximum cross correlation of the free run and observations. E - map of difference~~ DA; Column 4: MCC between ~~P90 of the free run and~~ observations ~~. F~~ and ~~G are maps of MCC and D_{P90} for the~~ forecast with ~~assimilation. Colobars below are given for deformation,~~ DA; Column 5: increase of MCC ~~and D_{P90}~~due to DA.

~~On the second day of forecast the difference between the observed and simulated deformation fields generally increases. Fig. ?? zooms on a smaller region (1500 × 1500 km) in the central Arctic and shows that in some areas~~ The impact of the ~~spatial correlation between deformation fields decreases (dark blue arrows on~~ assimilation on the areas outside of the satellite data coverage can be illustrated on two examples with assimilation of real (Fig. 4) and synthetic (Fig. ~~??.F) , whereas in other areas it stays high (green arrows on Fig. ??.F) . This example was chosen to demonstrate that the deformations extrapolated by the model out of the region with assimilated data may compare well with observations on the next day of forecast (red circle on Fig. ??.F), but sometimes may become different (yellow circle on Fig. ??.F).~~ 5) data. These observations were assimilated in a limited area (indicated by grey colour on the respective figures) on 22 January and the forecast was compared to observations (area-limited satellite observations or pan-Arctic synthetic observations) on 23 January. Visual comparison of forecasts and observations, as well as the maps of MCC increase show that the correlation has improved not only in the area covered by the assimilated observations but also outside it.

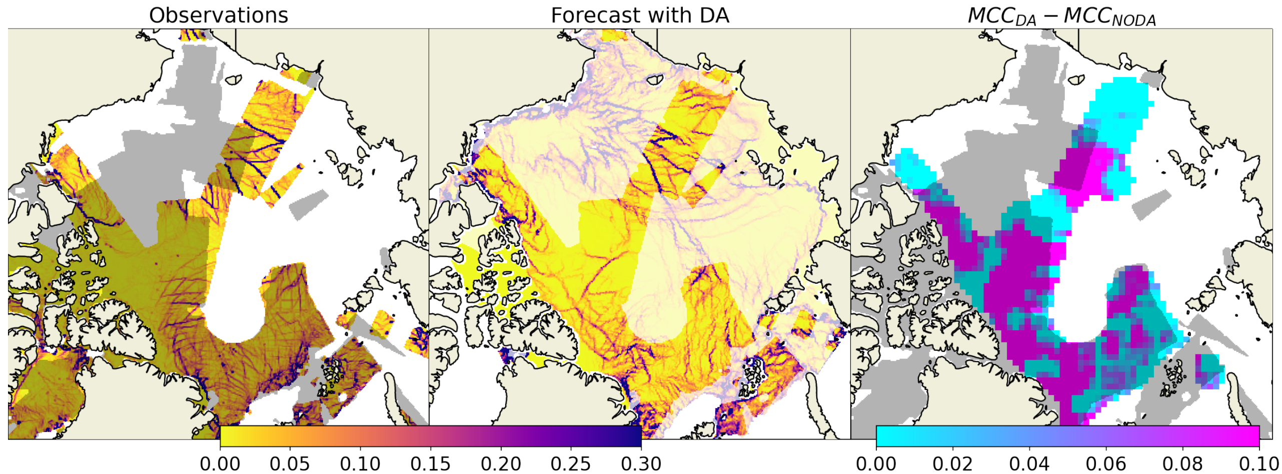

Figure 4. Maps of ~~deformation on observations~~ observed (~~A, D~~left panel) and ~~forecasts~~ simulated (~~B, E~~centre panel) ~~for 22 January (A, B) and for~~ deformation on 23 January 2021 and increase of maximum cross-correlation due to DA (~~D, E~~right panel). ~~Maps~~ The grey area on ~~C and F show maximum cross correlation computed in~~ the ~~sliding window. Red polygon on E~~ left and right panels shows the extent of ~~observations~~ data assimilated on ~~the previous day. Green arrows on F show where MCC stays high. Yellow and red circles on F show where extrapolated deformation is low or high, correspondingly. Colobars are the same as on Fig. ??.~~22 January 2021.

~~The evaluation metrics A_{MCC} and D_{P90}~~

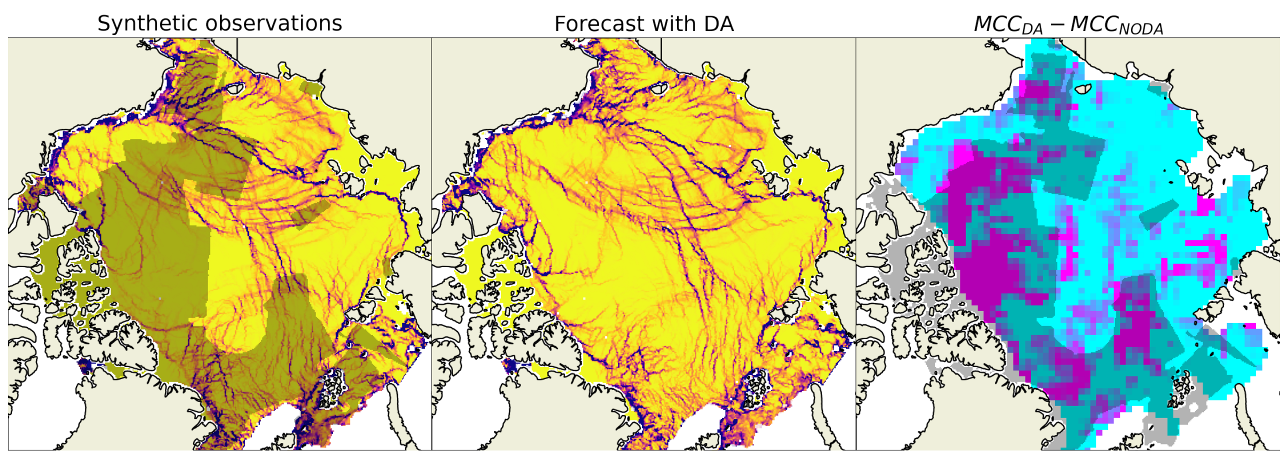

Figure 5. Same as Fig. 4 but for synthetic observations.

4.3 Practical predictability

The errors $\epsilon^T_{\delta t}$, ϵ_B, ϵ_Q, $\epsilon^S_{\delta t}$ and $\epsilon^A_{\delta t}$ were computed for each ~~day of the~~ forecast and averaged over 31 forecasts~~as well as for a free run and for the persistent forecast. In the persistence forecast the analysis from the first day is compared to observations from consecutive days. The metrics were averaged and plotted against lead time as~~. The errors with lead time (shown on

Fig. 6. Comparison of the metrics shows that the free run deformations are quite different from the observations — only ∼) evolve as expected (as in Fig. 1) — the forecast initiated from the truth run has the lowest error, which grows slower than those from the other forecasts. The error $\epsilon^T_{\delta t}$ does not reach the background level ϵ_B, and we can conclude that the intrinsic predictability is larger than 10 % of the area has sufficiently high correlation and the difference in deformation P90 is above 0.13 day^{-1}. Assimilation substantially improves the correspondence to the observations: area covered by valid deformation exceeds 80% and D_{P90} drops to 0.06 days^{-1}. On the second day the area with correlated deformation drops to 30% and with lead time longer than days. In forecasts with assimilation of synthetic data the forecast error is initially larger and reaches the background on the 4th day, whereas in forecasts with assimilation of satellite observations the error has already reached the background level by the 3days it is almost indistinguishable from the free run. The difference of P90 does not increase that fast — it remains lower than the free run during the entire 5-day forecast. The error in the persistence forecast grows faster than in the dynamic forecast — by the fifth day the high correlation area is lower by 5% and the $D_{P()}$ is larger by 0.3 day^{-1rd} day. Thus, we can say that practical predictability is 4 and 3 days when assimilating synthetic and real observations (respectively).

These results indicate that assimilation of sea ice deformation has an impact over a period as long as 5 days. The exact position of the cracks is improved only during the first 1 - 1.5 days, but the pan-Arctic spatial distribution is improved over longer time scales.

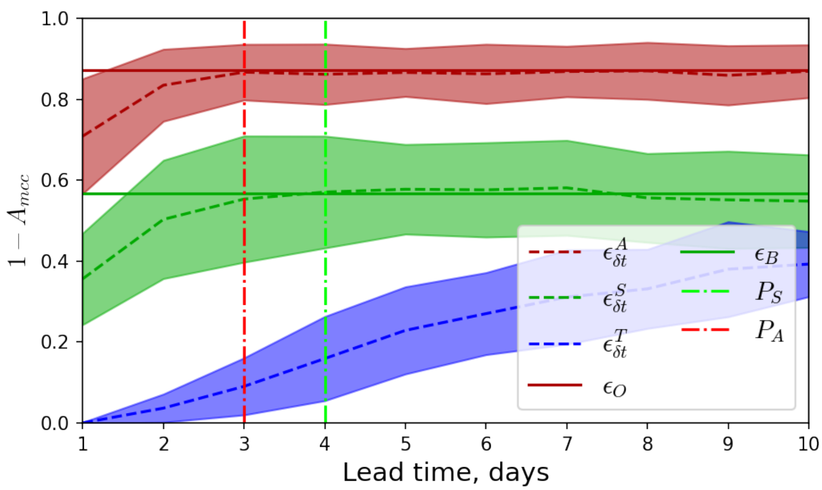

Figure 6. Evolution of errors of the area with high correlations (A) and root mean square difference (B) averaged over 31 days for the forecasts(green), persistence (blue) . Line styles and the free run (red)colouring correspond to Fig. Filled region 1, the filled area shows one quarter of standard deviation.

4.4 Sensitivity to assimilation parameters

The sensitivity experiments with the results of the sensitivity experiments are summarised on Fig. 7, where the dependence of forecast error (presented as $1 - A_{MCC}$ and KS) on values of the assimilation parameters is presented for the first three days of the forecasts. The results show that the forecast error is very sensitive to the a_1 ~~parameter of our assimilation scheme show that during the first day of forecast the minimum D_{P90} (~0.06) and maximum A_{MCC} (~0.8) are observed when a_1 values are in the range of -1.5 – -0.9 (see Fig. 7). A value of a_1 = -1 corresponds to linear reduction in concentration due to pure divergence, therefore for sufficient effect of assimilation the concentration needs to be decreased slightly more when computed from the total deformation~~and w_c parameters, is somewhat sensitive to the ε_{min} parameter, but has almost no sensitivity to the w_d parameter. In other words, assimilation of damage has little impact on forecast error, whereas assimilation of concentration plays a big role.

With ~~higher a_1 the error is higher both on the first and on the consequent days of forecasts (up to the level of free run, D_{P90} = 0.12, A_{MCC} = 0.15),~~ $a_1 = 0$ or $w_c = 0$ the $1 - A_{MCC}$ error is the highest and increasing a_1 or w_c leads to decrease of this error, indicating that the ~~impact of assimilation is too weak. With higher a_1, the error is higher on the first forecast day but is close to the minimum on the second and third days. That demonstrates the impact of excessive concentration nudging, which exaggerates deformations~~ stronger the inserted reduction of concentration, the large the correlation between forecasts and observations. However, if the concentration is modified too much during the assimilation ($a_1 > 1$ and $w_c > 0.5$) the forecast deformation increases in magnitude too much and the KS error also starts to grow fast. The forecasts with lead times of 1 day are most impacted, but similar dependencies are also visible in forecasts with lead times of 2 and 3 days.

Increasing the ε_{min} parameter leads to a slow increase of both the $1 - A_{MCC}$ and KS errors, particularly on the first day ~~but keeps the information on cracks for a longer time.~~

~~Several experiments with ε_{min} show~~ of forecast. It can be concluded that even very spatially localized assimilation, when ε_{min} = 0.1, quite considerably impacts the ~~field of deformations~~fields of deformation: the quality is only slightly lower than in the forecasts with ε_{min} = 0.02~~(D_{P90} higher by 0.1, A_{MCC} lower by 0.1)~~.

~~The experiments with~~

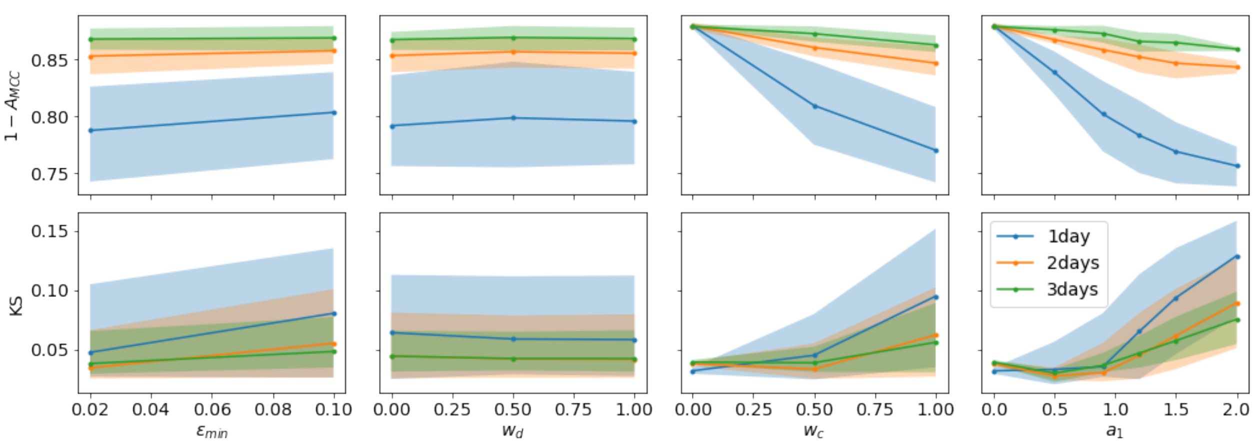

Figure 7. Dependence of the errors ($1 - A_{MCC}$ and KS) on the assimilation parameters. The solid lines show averages over all experiments and filled areas show 1 standard deviation. Colours denote different lead times.

For selecting the best parameters we plot their values against the quality metrics $1 - A_{MCC}$ and KS on Fig. 8 for each individual experiment. These scatter-plots show:

- that $1 - A_{MCC}$ is inversely proportional to KS, i.e., with higher correlation the difference in the probability distributions of the total deformation is also larger.
- $\varepsilon_{min} = 0.02$ provides better results almost in all experiments.
- w_d ~~cannot detect a strong impact of damage assimilation. With $w_d = 1$, the quality is only marginally better: D_{P90} lower by 0.01, A_{MCC} higher by 0.01).~~ has no impact on the metrics.
- $w_c = 1$ provides the best results when a_1 is 0.9 or 1.2.
- Decrease in w_c can be somewhat compensated by increase in a_1, but the results are still worse than with $w_c = 1$.

Based on these observations the following values were chosen as the recommended ones: $\varepsilon_{min} = 0.02$, $w_d = 1$, $w_c = 1$, $a_1 = 0.9$.

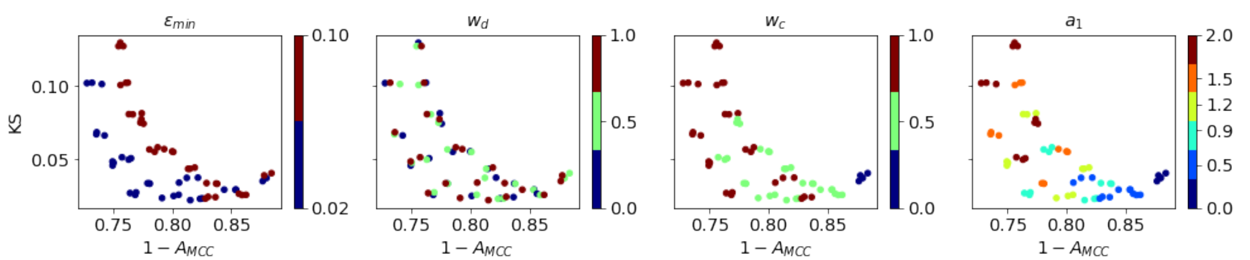

Figure 8. ~~Dependence~~ Results of ~~the averaged~~ individual sensitivity experiments as scatter-plots of $1 - A_{MCC}$ error ~~metrics (D_{P90}~~ on X-axis and ~~A_{MCC})~~ KS error on ~~parameters~~ Y-axis with values of ~~assimilation~~parameters shown by color.~~Red: ε_{min} = 0.1 (localized impact), w_d = 0; Green: ε_{min} = 0.02 (wide impact), w_d = 0; Blue: ε_{min} = 0.1 (localized impact), w_d = 1; Yellow: ε_{min} = 0.02 (wide impact), w_d = 1. Bars with a_1 = 0 illustrate experiments with damage assimilation only.~~

5 Discussions

5.1 Theoretical and practical usefulness

We present the first successful attempt to use ~~the~~ observed sea ice deformation to ~~improve sea ice model prediction skills on a horizon of 3–5~~ increase accuracy of deformation prediction for the first $2 - 3$ days. The approach we used to update the model fields is relatively simple ~~- the simulated values of sea ice~~ — the concentration and damage are ~~nudged towards the concentration and damage~~ computed from the observed ~~ice deformation. In addition, we~~ sea ice deformation and inserted into the simulated fields using weighted averaging. We use this simplified ~~nudging~~ data insertion scheme with only a few tuning parameters, instead of using more sophisticated DA methods such as the EnKF, for the sake of confirming several hypotheses and providing a proof of concept. First, it Our study demonstrates in practice that information contained in the observed deformation fields can be related to the used for initialisation of model state variables. Second, it , and shows the time scales at over which the forecast of deformation can be improvedby updating some model variables. Third, it proves . Our experiments illustrate that even if nudging data insertion is spatially limited by satellite observations (or even very localized in high deformation zones) it corrects can realistically extrapolate the deformation pattern simulated with the neXtSIM model in the entire basinby connecting the elements of linear kinematic features. Finally, it reveals the relative importance of the assimilation parameters (e.g., a_1 vs. ε_{min}) and, as explained below, the relative importance of the model state variables is revealed.

The experiments, in which we minimized the difference between simulation and observations by tuning the parameters in a grid search, can be interpreted as an optimization of the DA hyperparameters. These parameters can be associated with uncertainties in observed deformation, which are either spatially constant (a_1, w_c and w_d), or spatially varying (ε_{min}). These uncertainties can be related to the diagonal terms in the error covariance matrices used in more sophisticated EnKF and 4DVar methods. However, the uncertainty of the model concentration and damage is either not known or not taken into account. Further study is needed to derive a full covariance matrix, especially the off-diagonal terms depicting cross-variable relations. Knowledge of this obvious weakness in the presented approach paves the road for the planning of future experiments: an ensemble of neXtSIM runs (with perturbed forcing) should be used for evaluating uncertainties in the model variables; detection of covariance between the observed deformation and the model state (not restricting to just damage and concentration); and eventually updating the model state using state-of-the-art DA techniques.

From the practical point of view, the presented approach is useful for the current realisation of the forecasting platform neXtSIM-F. neXTSIM-F is currently used operationally for providing sea ice forecasts through CMEMS. For now, the platform can only operate with a single neXtSIM member but is outfitted with full functionality required for operational work: download of forcing and observations data, assimilation of sea ice concentration and type, running of the model, visualisation and validation of the forecasts. Integration of the suggested assimilation approach into neXtSIM-F will improve forecasts of sea ice leads and ridges, providing information that is crucial for tactical navigation in the Arctic.

5.2 Impact of damage and concentration assimilation

As indicated in Olason et al. (2022), neXtSIM is a damage propagation sea ice model and damage is used for changing elasticity and viscosity. So why can't we see the impact of damage assimilation in our experiments? We believe there are two major reasons for that. First, the damage is acting in the model at much smaller timescales than our observations of sea ice deformation. Damage can increase from 0 to 1 in just a few model steps before it eventually starts to decay due to a mechanical healing mechanism. The increase of damage takes only a few minutes of simulated time, during which apparent sea ice elasticity and viscosity are proportionally decreased and large-scale and permanent deformation is allowed, accompanied by sea ice internal stresses relaxation. The available observations of deformation are taken on time scales of 24 hours and cannot detect such rapid processes.

The hypothesis that concentration and damage act on different time scales was tested in an idealised twin-experiment: an initially intact ice field ($d = 0$ and $A = 1$ everywhere) was 'broken up' along realistic LKFs. In one experiment, the elements in the LKFs were initiated by reducing concentration to 0.65 and in another one - by increasing damage to 1. The evolution of damage and concentration in several thousand elements of broken-up and intact ice was studied (see Fig. 9).

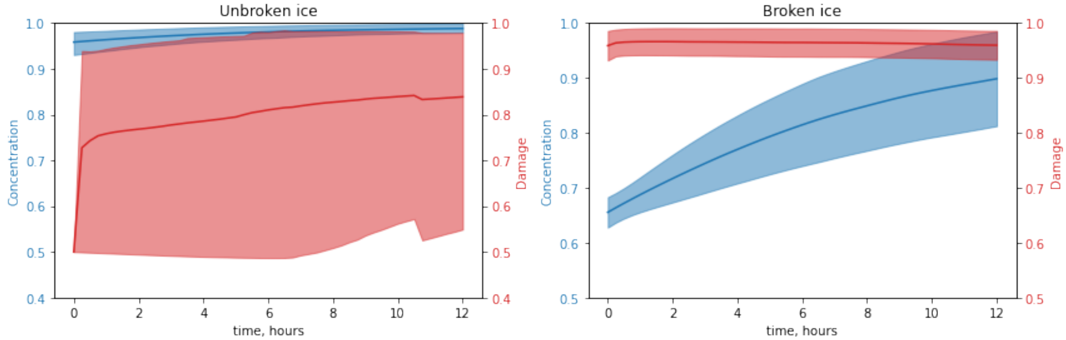

Figure 9. Mean and standard deviation of damage (red) and concentration (blue) in intact (left) and broken-up (right) elements.

The study shows that in case when LKFs are initiated by reduced concentration the situation is quite simple: concentration of ice in the unbroken elements is stably high, and in the broken elements it is first low and then stably increasing due to freezing (and convergence).

For damage the situation is quite different: in the initially unbroken elements the average damage remains relatively low (0.7 - 0.85), but damage variations are very large with standard deviation reaching 0.2. This happens because in some unbroken elements, that surround the initiated cracks, the internal stress exits the Mohr-Coulomb envelope and damage increases up to 1 at very short time scales (few time steps as discussed below, Fig. 10). Further, a cascade of damage events occurs in the neighbours of these newly broken elements. Probability of a break up (damage increase) is higher in directions of high internal stress. Thus, the information about the initiated damage is almost instantly forgotten — it is masked by many newly damaged elements.

Large scale observations of deformation at hourly frequency could probably confirm or reject the hypothesis of how damage propagates in reality, and illustrate whether or not assimilation of damage indeed leads to a more accurate deformation field **on small time scales**. However, we assimilate and validate against daily observations that show only long term memory in ice weakness expressed in reduced ice concentration.

The second reason is that the BBM rheology assumes the ice to be a two-phase material. One phase is that of small deformations, permitted by increasing damage, and the other is of large deformations, permitted by decreasing concentration. Damage linearly impacts the ice stiffness, whereas the ~~concentration acts in the exponent~~ stiffness has an exponential dependance on concentration (see Eqs. 2 and 3). In a compact ice cover the ice can only deform by first damaging. If this deformation is mainly convergent the concentration stays high and the deformations remain small. If, on the other hand the flow diverges, concentration drops and the deformations can become large.

These considerations can be illustrated by looking at what happens in two distinct elements that we picked up from the free run from the model mesh at different locations of the integration domain (see Fig. 10). In the first element (blue lines on Fig. 10) the normal and tangent stresses grow until they reach the Mohr-Coulomb envelope, when the damage starts to build up (we are interested in the second event). When damage reaches 0.75 (indicated by the blue dashed line) a small jump in the total deformation is observed and the stresses are relaxed on the next step. However the deformation was not large enough to sufficiently decrease the concentration and therefore the later remains close to 100%. This means that even if the damage reaches high values in this particular mesh element, the deformation remains low. In the second element (orange lines on Fig. 10) the initial deformation at the break-up event is larger, the concentration decreases rapidly and, as a result, the deformation on later steps reaches much higher values.

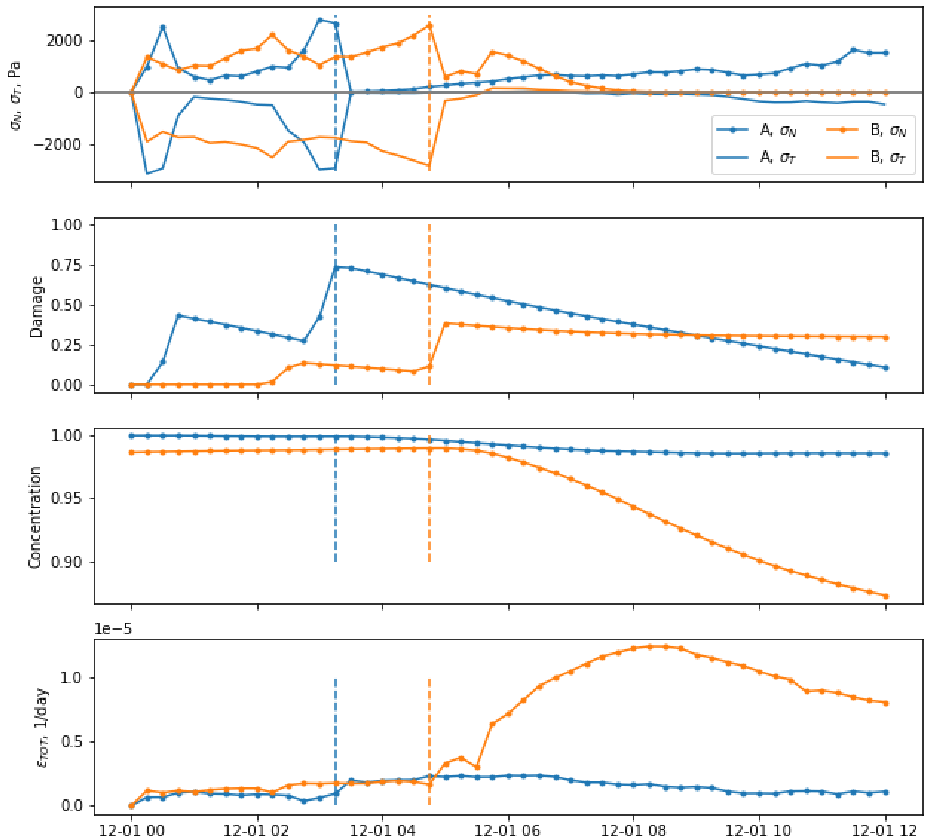

Figure 10. Evolution of internal stress (σ_N and σ_T), damage (d), concentration (A) and total deformation (ε_{tot}) in two independent elements (blue and orange lines). Vertical lines show approximately the time of ice break-up.

5.3 Towards evaluation of short-term sea ice predictability

How predictable sea ice features are at kilometre and daily time scale scales still remains an open question. Mohammadi-Aragh et al. (2018) gives a first estimate of the potential predictability of LKFs to be 4–8 days using MITgcm ensemble runs perturbed with atmospheric conditions from the ECMWF Ensemble Prediction System. They also found that additional perturbations in the initial sea ice thickness initial conditions do not contribute significantly to the forecast error growth in LKFs. The current study provides a new predictability estimate in a different context. Our results show that the deterministic forecast of LKFs gains prediction skill for 2–5 days after assimilating deformation observations, indicating a clear impact of improving accuracy of sea ice initial conditions. The viscous-plastic (VP) rheology used in MITgcm is known to have a less realistic slower time evolution of LKFs (Hutter et al., 2018) than the BBM rheology in neXtSIM (Olason et al., 2022). As a result, the sea ice simulated by the BBM rheology has more rapid error growth (loses skill faster) due to the correctly resolved intermittent ice motion and localised ice deformation.

In real world application, the prediction skill of sea ice LKFs depends on several sources of uncertainties /deficiencies in the system (listed below), so further studies are needed to address each of them and to build a complete picture of the current prediction skill of sea ice at daily time scales and the room for future improvements.

- **Uncertainties in atmospheric and ocean forcing.** Accuracy of contemporary weather and oceans The accuracy of contemporary atmospheric and ocean forecasts is quite high (Zhang et al., 2019; Xie et al., 2017). Nevertheless, while forcing the ice model with slightly inaccurate wind fields or ocean currents may only slightly change the ice drift pattern, but the ice deformation, being a spatial derivative, will be affected more. Surface wind variability is an important source of sea ice uncertainties (Rabatel et al., 2018; Cheng et al., 2020). A recent study showed that increasing the accuracy (resolution) of atmospheric boundary condition will improve improves the representation of sea ice extreme breakup events in the neXtSIM during the passage of polar cyclones (Rheinlaender et al. in review). (Rheinlænder et al., 2022). More comprehensive studies are needed to evaluate the impact of external forcing uncertainties on sea ice LKF forecasts at daily time scales.

- **Rheology and model parameterization.** Uncertainties in rheology rheological parameters were shown to be another error source for sea ice forecasts (Urrego-Blanco et al., 2016; Cheng et al., 2020). The BBM rheology (Olason et al., 2022) was implemented in neXtSIM quite recently to replace the previous Maxwell Elasto-Brittle rheology of Dansereau et al. (2016). It was only calibrated to be compared to statistical properties of sea ice deformation derived from the RGPS observation dataset (Kwok et al., 1990) and on large-scale sea ice thickness and drift time series. Therefore, it is not , and has not yet been tuned for predicting the exact position of cracks in the sea ice cover, which may impact the predictability we obtain in this study. The BBM rheology can be further tuned and compared to the modified Elasto-Visco-Plastic rheology (mEVP, Bouillon et al., 2009) (mEVP, Bouillon et al., 2013) that is already an available option in neXtSIM (Olason et al., 2022) for estimating the impact of rheology on the sea ice predictability. We expect that the model equipped with the mEVP rheology will not be capable of spatial extrapolation of the assimilated ice weakness (lowered A or enhanced d), and that further tuning of the BBM rheology can improve the practical predictability of LKFs.

– **Model numerics.** In neXtSIM, the model equations are derived and solved on a triangular mesh that deforms with the ice motion in a pure-Lagrangian approach. In addition to the physics of the rheological model, this Lagrangian approach may contribute to improving the localisation of cracks in space and time. However, in ~~such~~ this framework a remeshing procedure is used when the mesh becomes too distorted in order to replace too skewed triangles with nearly isosceles triangles. After the remeshing procedure, the model variables are interpolated from the old to the new mesh using a conservative interpolation via supermesh construction. This results in a diffusion of the model fields and likely impacts the ~~prediction~~ predictive skill of the model. Ongoing work of implementing the BBM rheology in an Eulerian version of the neXtSIM model, using a Discontinuous Galerkin advection scheme, will allow us to study the impact of the use of a fixed Eulerian grid compared to a Lagrangian mesh on the efficiency of the data assimilation method and sea ice deformation predictability.

– **Initial conditions for sea ice states.** The impact from ~~initial condition uncertainties~~ uncertainties in initial conditions can be revisited using ~~the~~ neXtSIM with the new BBM rheology. Future studies ~~can~~ could run ensembles of neXtSIM simulations with perturbation of ice thickness (mean or distribution), concentration, damage, ~~ice types and the ice thickness distribution~~ and ice type variables to assess propagation of errors ~~across variables and scales and~~ between variables and across scales and to evaluate their impact on predictability.

– **~~Observing~~ Observation network and data assimilation** In practice, the choice of DA method and availability of observations will also impact the accuracy of initial conditions and therefore impact the predictability. In this study, we made a first attempt to assimilate deformation derived from the operationally available sea ice drift product from ~~CMEMS~~Copernicus Marine Services, which provides information at ~~the smaller~~ daily time scales for sea ice features. Future studies can assess how observations on different scales (e.g. with higher spatial and temporal resolution) impact the predictability. Also, DA performance can be further improved in future studies using more sophisticated methods to further improve the accuracy in initial conditions.

6 Conclusions

The presented method for assimilation of satellite-derived sea ice deformation into the neXt generation Sea Ice Model (neXtSIM) efficiently ~~ingests~~ inserts information about where the ice is mechanically weak and improves forecasts of ice deformation for ~~a horizon of 3–5~~ the first 2 – 3 days. Despite using a relatively simple ~~nudging~~ data insertion approach, neXtSIM is capable of extrapolating the spatially discontinuous satellite observations of deformation by connecting the elements of linear kinematic features in a realistic manner. The main idea behind the proposed method is to relate local sea ice weakness to local reduced ice concentration and increased ice damage, which are computed as functions of observed ice deformation. Experiments with the parameters of the DA scheme show that updating concentration substantially improves neXtSIM skills on the synoptic scale, whereas updating damage has an effect only on time scales of a few hours, which is difficult to confirm by satellite observations. It is anticipated that update of the ice damage with more frequent observations will play a bigger role in increasing the accuracy of the short range forecasts~~to fully take advantage of the brittle rheology~~. The presented approach can already be used in operational forecasting systems for improving deterministic forecasts, or it can be developed further and integrated into a variational assimilation approach based on ensemble runs.

Data availability. TOPAZ4 ocean forcing data and Sea ice deformation data is publicly available at the Copernicus Marine Cervices portal:

- https://resources.marine.copernicus.eu/product-detail/ARCTIC_ANALYSIS_FORECAST_PHYS_002_001_a/
- https://resources.marine.copernicus.eu/product-detail/SEAICE_GLO_SEAICE_L4_NRT_OBSERVATIONS_011_006/

ECMWF atmosphere forcing data is available on the ECMWF website: https://www.ecmwf.int/en/forecasts/datasets.

neXtSIM code used in the present manuscript is not publicly available.

The forecasts are available per request.

Author contributions. This work is based on an original idea of PR. AK, PR and YY designed the methodology and AK carried out the simulation experiments and the analyses. EO, TW, PR and AK developed the neXtSIM model code. AK prepared the manuscript with contributions from all co-authors.

Competing interests. The authors declare that they have no conflict of interest.

Acknowledgements. This study was supported by the following projects: ImpSim funded by the Service hydrographique et océanographique de la marine (SHOM), MOIRA funded by the European Space Agency (ref.no. 4000129593/19/I-DT), and MUSIC funded by the Norwegian Research Council (ref.no. 325292 - FORSKER21). We thank to the Copernicus Marine Environmental Cervices for providing the sea ice drift and deformation data product. We also thank Sylvain Bouillon for the numerous discussions that ~~lead to the idea developed in~~ motivated this study.

References

Amitrano, D., Grasso, J. R., and Hantz, D.: From diffuse to localised damage through elastic interaction, Geophys. Res. Lett., 26, 2109–2112, 1999.

Bouchat, A., Hutter, N. C., Chanut, J., Dupont, F., Dukhovskoy, D. S., Garric, G., Lee, Y. J., Lemieux, J.-F., Lique, C., Losch, M., and et al.: Sea Ice Rheology Experiment (SIREx), Part I: Scaling and statistical properties of sea-ice deformation fields, Earth and Space Science Open Archive, p. 36, https://doi.org/10.1002/essoar.10507397.1, 2021.

Bouillon, S. and Rampal, P.: Presentation of the dynamical core of neXtSIM, a new sea ice model, Ocean Modelling, 91, 23–37, https://doi.org/10.1016/j.ocemod.2015.04.005, 2015a.

Bouillon, S. and Rampal, P.: On producing sea ice deformation data sets from SAR-derived sea ice motion, The Cryosphere, 9, 663–673, https://doi.org/10.5194/tc-9-663-2015, 2015b.

Bouillon, S., Ángel Morales Maqueda, M., Legat, V., and Fichefet, T.: An elastic–viscous–plastic sea ice model formulated on Arakawa B and C grids, Ocean Modelling, 27, 174–184, https://doi.org/10.1016/j.ocemod.2009.01.004, 2009.

Bouillon, S., Fichefet, T., Legat, V., and Madec, G.: The elastic–viscous–plastic method revisited, Ocean Modelling, 71, 2–12, https://doi.org/10.1016/j.ocemod.2013.05.013, 2013.

Brunelli, R.: Template Matching Techniques in Computer Vision: Theory and Practice, Willey, 2009.

Cheng, S., Aydoğdu, A., Rampal, P., Carrassi, A., and Bertino, L.: Probabilistic Forecasts of Sea Ice Trajectories in the Arctic: Impact of Uncertainties in Surface Wind and Ice Cohesion, Oceans, 1, 326–342, https://doi.org/10.3390/oceans1040022, 2020.

Colony, R. and Thorndike, A. S.: An estimate of the mean field of Arctic sea ice motion, Journal of Geophysical Research, 89, 10 623, https://doi.org/10.1029/JC089iC06p10623, 1984.

Dansereau, V., Weiss, J., Saramito, P., and Lattes, P.: A Maxwell elasto-brittle rheology for sea ice modelling, The Cryosphere, 10, 1339–1359, 2016.

Dierking, W., Stern, H. L., and Hutchings, J. K.: Estimating statistical errors in retrievals of ice velocity and deformation parameters from satellite images and buoy arrays, The Cryosphere, 14, 2999–3016, https://doi.org/10.5194/tc-14-2999-2020, 2020.

EUMETSAT: Ocean and Sea Ice Satellite Application Facility, AMSR2 sea ice concentration, https://osisaf.met.no/quicklooks/prod/ice/2021/01/ice_conc_nh_polstere-100_amsr2_202101161200_qlook.png, last accessed on 1 Nov 2021, 2021.

Evensen, G.: The Ensemble Kalman Filter: theoretical formulation and practical implementation, Ocean Dynamics, 53, 343–367, https://doi.org/10.1007/s10236-003-0036-9, 2003.

Girard, L., Bouillon, S., Weiss, J., Amitrano, D., Fichefet, T., and Legat, V.: A new modeling framework for sea-ice mechanics based on elasto-brittle rheology, Annals of Glaciology, 52, 123–132, https://doi.org/10.3189/172756411795931499, 2011.

Hopkins, M. A.: Four stages of pressure ridging, Journal of Geophysical Research: Oceans, 103, 21 883–21 891, https://doi.org/10.1029/98JC01257, 1998.

Hutter, N., Losch, M., and Menemenlis, D.: Scaling Properties of Arctic Sea Ice Deformation in a High-Resolution Viscous-Plastic Sea Ice Model and in Satellite Observations, Journal of Geophysical Research: Oceans, 123, 672–687, https://doi.org/10.1002/2017JC013119, 2018.

Hutter, N., Zampieri, L., and Losch, M.: Leads and ridges in Arctic sea ice from RGPS data and a new tracking algorithm, The Cryosphere, 13, 627–645, https://doi.org/10.5194/tc-13-627-2019, 2019.

Korosov, A. and Rampal, P.: A Combination of Feature Tracking and Pattern Matching with Optimal Parametrization for Sea Ice Drift Retrieval from SAR Data, Remote Sensing, 9, 258, https://doi.org/10.3390/rs9030258, 2017.

Kwok, R.: The RADARSAT Geophysical Processor System, https://doi.org/10.1007/978-3-642-60282-5_11, 1998.

Kwok, R.: Deformation of the Arctic Ocean sea ice cover between November 1996 and April 1997: a qualitative survey, Solid Mechanics And Its Applications, 94, 315–322, 2001.

Kwok, R., Curlander, J., McConnell, R., and Pang, S.: An ice-motion tracking system at the Alaska SAR facility, IEEE Journal of Oceanic Engineering, 15, 44–54, https://doi.org/10.1109/48.46835, 1990.

Lindsay, R. W. and Stern, H. L.: The RADARSAT Geophysical Processor System: Quality of Sea Ice Trajectory and Deformation Estimates, Journal of Atmospheric and Oceanic Technology, 20, 1333–1347, https://doi.org/10.1175/1520-0426(2003)020<1333:TRGPSQ>2.0.CO;2, 2003.

Lorenc, A. C.: Analysis methods for numerical weather prediction, Quarterly Journal of the Royal Meteorological Society, 112, 1177–1194, https://doi.org/10.1002/qj.49711247414, 1986.

Marsan, D., Stern, H., Lindsay, R., and Weiss, J.: Scale Dependence and Localization of the Deformation of Arctic Sea Ice, Physical Review Letters, 93, 178 501, https://doi.org/10.1103/PhysRevLett.93.178501, 2004.

Mohammadi-Aragh, M., Goessling, H. F., Losch, M., Hutter, N., and Jung, T.: Predictability of Arctic sea ice on weather time scales, Scientific Reports, 8, 6514, https://doi.org/10.1038/s41598-018-24660-0, 2018.

Olason, E., Rampal, P., and Dansereau, V.: On the statistical properties of sea-ice lead fraction and heat fluxes in the Arctic, The Cryosphere, 15, 1053–1064, https://doi.org/10.5194/tc-15-1053-2021, 2021.

Olason, E., Boutin, G., Korosov, A., Rampal, P., Williams, T., Kimmritz, M., Dansereau, V., and Samaké, A.: A New Brittle Rheology and Numerical Framework for Large-Scale Sea-Ice Models, Journal of Advances in Modeling Earth Systems, 14, e2021MS002 685, https://doi.org/10.1029/2021MS002685, 2022.

Owens, R. G. and Hewson, T.: ECMWF Forecast User Guide, https://doi.org/10.21957/m1cs7h, 2018.

Rabatel, M., Rampal, P., Carrassi, A., Bertino, L., and Jones, C. K. R. T.: Impact of rheology on probabilistic forecasts of sea ice trajectories: application for search and rescue operations in the Arctic, The Cryosphere, 12, 935–953, https://doi.org/10.5194/tc-12-935-2018, 2018.

Rampal, P., Weiss, J., and Marsan, D.: Positive trend in the mean speed and deformation rate of Arctic sea ice, 1979–2007, Journal of Geophysical Research, 114, C05 013, 2009.

Rampal, P., Bouillon, S., Ólason, E., and Morlighem, M.: NeXtSIM: A new Lagrangian sea ice model, Cryosphere, 10, 1055–1073, https://doi.org/10.5194/tc-10-1055-2016, 2016.

Rampal, P., Dansereau, V., Ólason, E., Bouillon, S., Williams, T., Korosov, A., and Samaké, A.: On the multi-fractal scaling properties of sea ice deformation, The Cryosphere, 13, 2457–2474, https://doi.org/10.5194/tc-13-2457-2019, 2019.

Rheinlænder, J. W., Davy, R., Olason, E., Rampal, P., Spensberger, C., Williams, T. D., Korosov, A., and Spengler, T.: Driving Mechanisms of an Extreme Winter Sea Ice Breakup Event in the Beaufort Sea, Geophysical Research Letters, 49, e2022GL099 024, https://doi.org/10.1029/2022GL099024, 2022.

Sakov, P., Counillon, F., Bertino, L., Lisæter, K. A., Oke, P., and Korablev, A.: TOPAZ4: An ocean sea ice data assimilation system for the North Atlantic and Arctic, Ocean Sci., 8, 633–662, 2012.

Saldo, R.: Global Ocean - High Resolution SAR Sea Ice Drift, https://resources.marine.copernicus.eu/product-detail/SEAICE_GLO_SEAICE_L4_NRT_OBSERVATIONS_011_006/INFORMATION, https://doi.org/10.48670/moi-00135, 2020.

Smirnov, N.: On the Estimation of Discrepancy between Empirical Curves of Distribution for Two Independent Samples, Bulletin Mathématique de L′Université de Moscow, 2, 3–11, 1939.

Stanev, E. and Schulz-Stellenfleth, J.: Methods of data assimilation, Die Küste, 81, 133–151, https://doi.org/https://hdl.handle.net/20.500.11970/101688, 2014.

Sverdrup, H. U.: Physical Oceanography of the North Polar Sea, Arctic, 3, 178–186, 1950.

Urrego-Blanco, J. R., Urban, N. M., Hunke, E. C., Turner, A. K., and Jeffery, N.: Uncertainty quantification and global sensitivity analysis of the Los Alamos sea ice model, Journal of Geophysical Research: Oceans, 121, 2709–2732, 2016.

Williams, T., Korosov, A., Rampal, P., and Ólason, E.: Presentation and evaluation of the Arctic sea ice forecasting system neXtSIM-F, The Cryosphere, 15, 3207–3227, https://doi.org/10.5194/tc-15-3207-2021, 2021.

Xie, J., Bertino, L., Counillon, F., Lisæter, K. A., and Sakov, P.: Quality assessment of the TOPAZ4 reanalysis in the Arctic over the period 1991–2013, Ocean Science, 13, 123–144, https://doi.org/10.5194/os-13-123-2017, 2017.

Zhang, F., Sun, Y. Q., Magnusson, L., Buizza, R., Lin, S.-J., Chen, J.-H., and Emanuel, K.: What Is the Predictability Limit of Midlatitude Weather?, Journal of the Atmospheric Sciences, 76, 1077–1091, https://doi.org/10.1175/JAS-D-18-0269.1, 2019.

Zuo, H., Balmaseda, M. A., Tietsche, S., Mogensen, K., and Mayer, M.: The ECMWF operational ensemble reanalysis–analysis system for ocean and sea ice: a description of the system and assessment, Ocean Science, 15, 779–808, https://doi.org/10.5194/os-15-779-2019, 2019.

Appendix 1. Inverse observational operators

Inverse observational operator for damage H'_d

The operator H'_d (Eq. 20) is established from the following considerations. A true relationship between deformation and model variables is multivariate and involves nonlinear dependencies on the external forcing: for example, even fully-damaged ice will not deform without winds or currents. Satellite observations and previous studies with the neXtSIM model show that the values of ice deformation follow a log-normal distribution (Marsan et al., 2004; Rampal et al., 2019). Our simulations (Fig. 11, A) show that a linear relationship can be established between damage and total deformation in log-log space, i.e.,

$$\log_{10}(k_1 + 1 - d) = k_2 + k_3 \log_{10}(\varepsilon_{tot}) \tag{25}$$

where k_2 and k_3 are linear regression coefficients and k_1 is a small offset to prevent damage from getting too close to 1 (a critical value that damage should never reach in progressive damage models; Amitrano et al., 1999).

The coefficients k_1, k_2 and k_3 are found empirically following two steps. First, both the damage (d) and the simulated deformation (ε_{tot}) are taken from the truth run and the preliminary parameters are found by the minimisation in Eq. 19. The scatter-plot on Fig. 11, B compares the simulated damage (in $\log_{10}(1-d)$ space) with the damage reconstructed from the simulated ε_{tot} using the inverse operator, showing reasonable agreement despite the aforementioned factors. The maps in Fig. 12 compare the simulated deformation, simulated damage and damage reconstructed from simulated deformation using H'_d, and show good agreement for large values of damage. In the range of low deformations, we note however that the agreement is not as good.

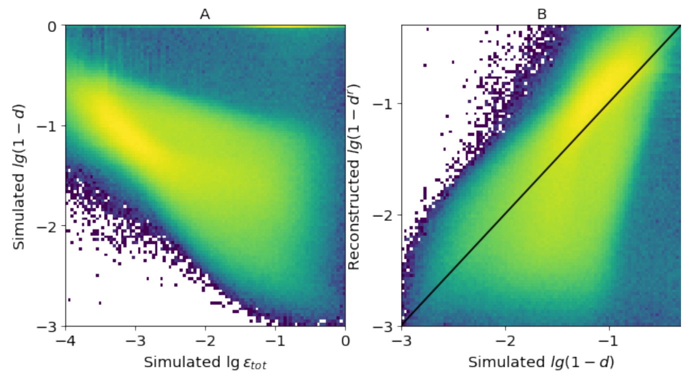

Figure 11. Comparison of simulated total deformation ε_{tot}, simulated damage d and damage reconstructed from simulated deformation d^r using Eq. 20. The black line on panel B shows 1-to-1 relation.

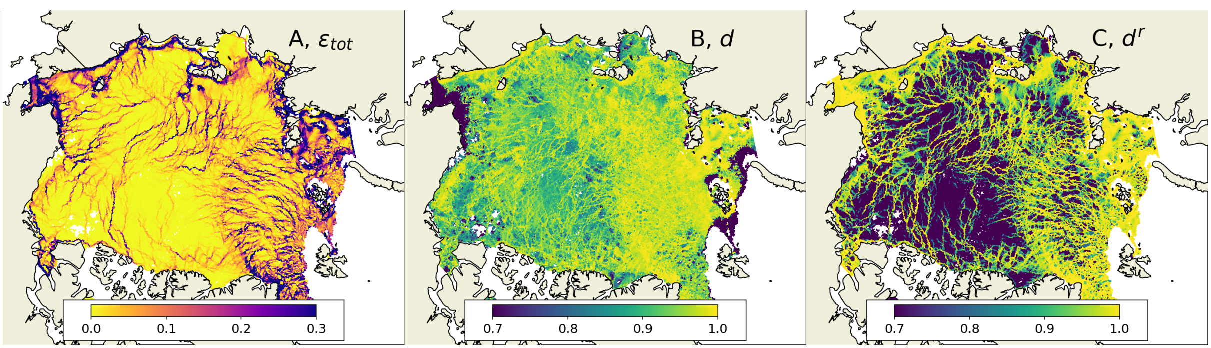

Figure 12. Comparison of maps of simulated total deformation ε_{tot}, simulated damage d and damage reconstructed from simulated deformation d^r for 5^{th} January 2020.

In the second step, the deformation is taken from satellite observations (ε^o_{tot}) and damage is derived by the inverse operator using the preliminary coefficients $d^o_1 = H'_d(\varepsilon^o_{tot})$. Comparison of the probability distribution functions (PDFs) of the simulated damage (d, blue area on Fig. 13) and the reconstructed damage (d^o_1, red line on Fig. 13) show deviations of PDFs due to the initial differences between the simulated and observed frequency distributions of deformation that result from varying integration time of satellite observations, noise in observations, and uncertainties in simulated ice drift. The coefficients k_1, k_2 and k_3 are updated in a semi-automatic multivariate minimisation of the difference between the PDFs and d^o_2 is computed using the updated H'_d (black line on Fig. 13). Values of the H'_d parameters after the two steps are given in Table 2, which shows that the histogram fitting changes the values only marginally.

Inverse observational operator for concentration H'_A

The simpler form of operator H'_A (Eq. 21) can be justified by the fact that decrease in concentration purely due to divergence can be given by an integral of the divergence rate (ε_{div}) over time, therefore the coefficient a_1 relates to the integration time.

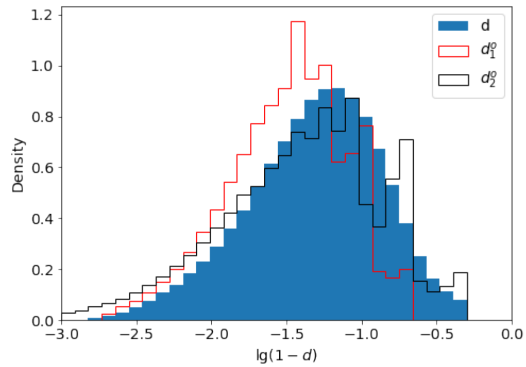

Figure 13. Comparison of probability density functions of simulated damage (d) and damage reconstructed from CMEMS observations of deformation using the first (d_1^o) and the second (d_2^o) sets of coefficient for H'_d.

Table 2. Parameters of H'_d operator after two steps of tuning.

	k_1	k_2	k_3
d_1^o	0.05	-2.7	-0.9
d_2^o	0.01	-3	-1.2

However, in Eq. 21, concentration is a function of ε_{tot} assuming that ice breaks and becomes weaker due to both convergence and shear. Therefore, Eq. 21 is not a strict relation and the parameter a_1 is derived empirically in the sensitivity experiments. An optimal value of a_1 is selected to keep both quality metrics A_{MCC} and KS as low as possible (see Sec. 4.4 and Fig. 8). Note, that unlike Eq. 19, the optimisation is performed here in the space of observations and using the observed total deformation.

The comparison of simulated deformation, simulated concentration and reconstructed concentration is provided on scatter-plots (Fig. 14) and on maps (Fig. 15). The overall agreement between simulated and reconstructed concentrations is good, but the simulated concentration is low only in areas where the divergence is high, whereas the reconstructed concentration is lower also in the areas with strong convergence or shear and represents weaker sea ice.

Appendix 2. Using maximum cross-correlation for comparing deformation fields

The satellite derived sea ice deformation field is a rasterized product with size 900×900 pixels and with spatial resolution of 10 km. The simulated sea ice deformation is computed on the model triangular mesh using contour integrals of the ice drift velocity (for details of deformation computation see Rampal et al., 2016, e.g.). Then the deformation field is rasterized - resampled from the model mesh to the grid of the satellite observations using a nearest-neighbour method. Comparison between the two gridded deformation products (e.g., derived from satellite observation and obtained from a simulation) is performed by computing maximum cross correlation (Brunelli, 2009) as explained below.

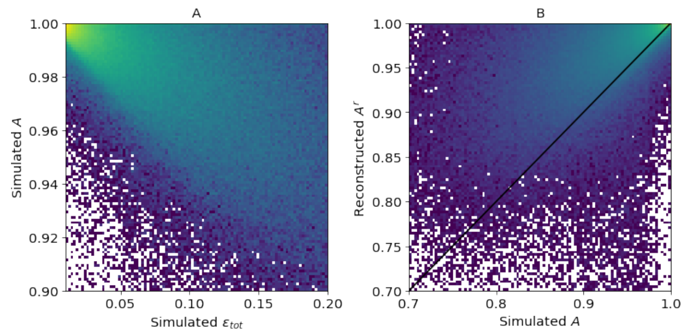

Figure 14. Comparison of simulated total deformation ε_{tot}, simulated concentration A and concentration reconstructed from simulated deformation A^r using Eq. 21. The black line on panel B shows 1-to-1 relation.

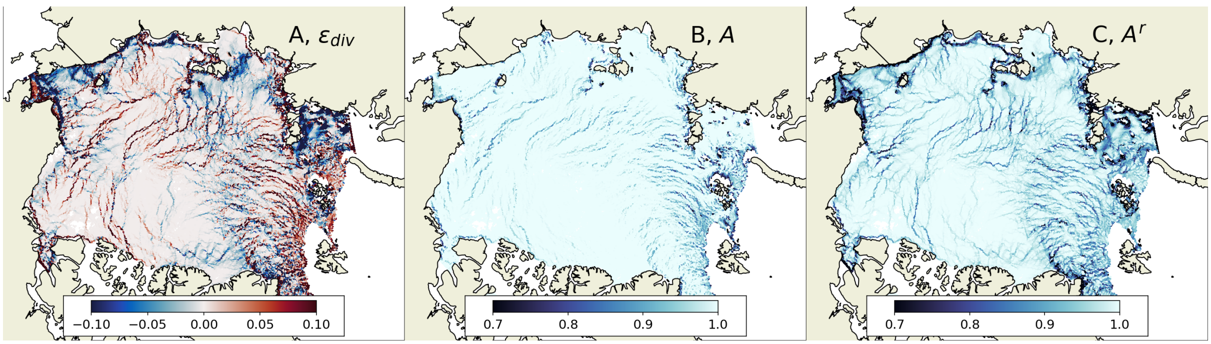

Figure 15. Maps of simulated divergence ε_{div}, concentration A and concentration reconstructed from simulated total deformation A^r for 5^{th} January 2020. The map of total deformation used for reconstruction of A^r is shown on Fig. 12.A.

The grid of the tested product is split into smaller square matrices of size $N \times N$ pixels (called the template), the grid of the reference product is split into slightly larger matrices (with size $K \times K$ pixels, called the image) with the same geographic location of the centre of the corresponding matrices. The cross-correlation matrix (CCM) between the template and the image is computed as follows (see also scheme on Fig. 16):

$$R(x,y) = \frac{\sum_{x',y'}(T'(x',y') \cdot I'(x+x',y+y'))}{\sqrt{\sum_{x',y'} T'(x',y')^2 \cdot \sum_{x',y'} I'(x+x',y+y')^2}}$$
$$T'(x,y') = T(x',y') - 1/(w \cdot h) \sum_{x'',y''} T(x'',y'')$$
$$I'(x,y') = I(x',y') - 1/(w \cdot h) \sum_{x'',y''} I(x'',y'') \tag{26}$$

where T is the template and I is the image, x' and y' are column/row coordinates of the centre of the image, x and y are column/row coordinates of the CCM.

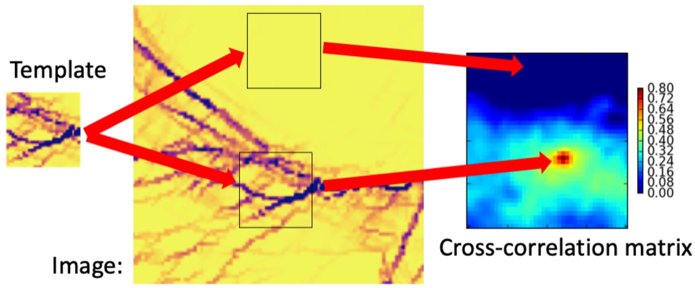

Figure 16. Scheme of computing the maximum cross correlation.

The maximum value from the CCM is used as a measure of similarity between the template and the image. The difference between the size of the template and the image ($(K-N)/2$) defines the tolerance of geographical misplacement of the tested and reference deformation fields. In our case we used template with size $K = 30$ pixels and image with size $N = 36$ pixels, meaning that a misplacement of 30 km was tolerated.